





RESEARCH ARTICLE | JUNE 14 2023

Global and local analyses of the Görtler instability in hypersonic flow

Special Collection: [Hypersonic Flow](#)

Uy Ken Chun Kit (黃駿傑) ; Hao Jiaao (郝佳傲)  ; Wen Chih-Yung (溫志湧) 



Physics of Fluids 35, 064111 (2023)

<https://doi.org/10.1063/5.0151349>



View
Online



Export
Citation

Global and local analyses of the Görtler instability in hypersonic flow

Cite as: Phys. Fluids **35**, 064111 (2023); doi: [10.1063/5.0151349](https://doi.org/10.1063/5.0151349)

Submitted: 21 March 2023 · Accepted: 31 May 2023 ·

Published Online: 14 June 2023



View Online



Export Citation



CrossMark

Ken Chun Kit Uy (黃駿傑), Jiaao Hao (郝佳傲), ^{a)} and Chih-Yung Wen (溫志湧)

AFFILIATIONS

Department of Aeronautical and Aviation Engineering, The Hong Kong Polytechnic University, Hung Hom, Kowloon, Hong Kong

Note: This paper is part of the special topic, Hypersonic Flow.

^{a)} Author to whom correspondence should be addressed: jiaao.hao@polyu.edu.hk

ABSTRACT

The stationary Görtler instability in hypersonic flow over a concave wall is systematically investigated across a range of geometric and flow parameters using resolvent analysis, which seeks for the forcing and response pair that maximizes the energy amplification. The optimal forcing takes the form of streamwise vortices, while the optimal response is streamwise streaks. The growth of the optimal disturbance is contributed by both the lift-up and centrifugal mechanisms. The latter becomes dominant as the boundary layer develops, and its growth rate agrees well with that predicted by local stability analysis. In terms of changes in geometric parameters, an increase in curvature destabilizes the Görtler instability, as expected, while the effect of the angle subtended by the concave wall (the turning angle) is shown to be negligible. With respect to changes in flow parameters, the Görtler instability is stabilized at low Reynolds numbers, destabilized under the cold-wall effect, and insensitive to the change in Mach number. The most amplified spanwise wavelength scales with the boundary-layer thickness, which remains mostly unchanged when the freestream Mach number is varied from 3 to 10. A new dimensionless wavelength parameter is proposed to predict the wavelength of the most dangerous Görtler vortices in the compressible flow regime. The resolvent analysis results are confirmed by a three-dimensional numerical simulation, where the hypersonic flow is perturbed by a spatial white noise.

Published under an exclusive license by AIP Publishing. <https://doi.org/10.1063/5.0151349>

I. INTRODUCTION

The Görtler instability is generated in the boundary layer over a concave surface due to the imbalance between the wall-normal pressure gradient and the centrifugal force and manifests itself as counter-rotating streamwise vortices. Extensive research has been conducted on this centrifugal instability in the incompressible flow regime.^{1–3} However, its compressible counterpart is also significant in contributing to the onset of transition along the walls of supersonic and hypersonic wind tunnels and the forebody compression surface ahead of the engine inlet on scramjet vehicles.⁴ Further investigation into this topic, particularly in hypersonic flows, is warranted.

There are only a few experimental studies on the Görtler instability in high-speed flows with curved surfaces. De Luca *et al.*⁵ measured spanwise heat transfer fluctuations using an infrared imaging system in a Mach 7.0 flow over a concave wall. Ciolkosz and Spina⁶ found that the wavelength of Görtler vortices over a concave wall was almost invariant with wall curvature and Mach number, in a range of Mach 1.0–3.0. More recently, Huang *et al.*^{7,8} conducted a series of experiments at Mach 6.5 and captured Görtler vortices that are either naturally developed or roughness-induced using Rayleigh scattering flow visualization.

The interaction of the Görtler vortices with Mack's second mode was addressed.⁹ These empirical findings illustrate the onset of Görtler instability in supersonic/hypersonic flows over a curved geometry, including the development of Görtler vortices and their secondary instability modes in the transition and breakdown stages to turbulence. In addition to the curved wall geometry, the Görtler vortices behavior can also be found experimentally in dual-incident shock-wave/turbulent-boundary-layer interactions.¹⁰

Numerical simulations have been adopted by various researchers to gain insight into the flow structure and underlying mechanisms of Görtler instability, including the secondary instability, on a curved plane. Whang and Zhong¹¹ simulated a case of Mach 15 flow over a blunt wedge with a concave surface and revealed the nonlinear structure of secondary Görtler instability. Ren and Fu¹² investigated the compressibility effect on the Görtler instability on a concave wall by covering a range of Mach numbers from incompressible to hypersonic flows, i.e., Mach 0.015–6.0, revealing that the temperature disturbance of the Görtler mode shifts from the wall to near the edge of the boundary layer when the flow becomes hypersonic. Chen *et al.*^{13,14} studied a curved wall geometry with an upstream flat plate at Mach 6.5, demonstrating

the coexistence of the Görtler and the Mack modes, and the breakdown process of the secondary Görtler instability under different spanwise wavelength excitation using wall blowing and suction. Song *et al.*¹⁵ explored the same curved wall geometry as Chen *et al.*¹³ and proposed that the secondary Görtler instability could be originated from the first/second Mack mode. More recently, this curved wall geometry has been used to investigate the stabilization effect on grooves on Görtler instability¹⁶ and the boundary layer transition induced by low-frequency blowing and suction.¹⁷ Li *et al.*¹⁸ examined a case of Mach 6 axisymmetric cone with a concave aft body and documented the existence of secondary instabilities in the context of stationary Görtler mode for the first time. Understanding the occurrence of the Görtler instability at the linear growth stage, particularly the modal/nonmodal amplification under different flow and geometric changes, is crucial to investigate its nonlinear development in various hypersonic flow conditions. In these studies, linear stability theory (LST) and parabolized stability equations (PSE) are commonly used to verify modal growth.

Theoretically, a unique neutral curve with the parallel flow assumption is often used in the local stability analysis. However, this uniqueness is not tenable if the wavelength of Görtler vortices is comparable to the boundary layer thickness, in which both the initial conditions and the nonparallel nature of the boundary layer contribute.^{19,20} The source of external disturbance denoting the initial condition in the formation of Görtler vortices includes the surface roughness²¹ and the freestream vortical disturbance.^{22–24} The local stability analysis is only applicable if the Görtler number G is large enough (e.g., $G > 7$ was reported by Bottaro and Luchini²⁵). Through the LST, the Görtler instability is shown to originate from the continuous spectrum of the vorticity/entropy wave.²⁶ The second Görtler mode is also present in the LST but is less important due to the lower amplification rate over the entire wavelength range.²⁷ The PSE is also useful in investigating the early stage of flow transition. However, this analysis is only valid for flows in which the root mean square of the variable profiles varies slowly in the streamwise direction.¹⁵ The effect of initial conditions on the Görtler instability is also discussed by Spall and Malik.²⁸ The initial-disturbance problem is eased by optimal growth analysis,^{29–32} which is established based on PSE and determines the optimal disturbances that maximizes the spatial growth. Optimal growth analysis was applied to the Görtler instability by Cossu *et al.*³¹ in incompressible flow and by Li *et al.*³² in hypersonic flow over an axisymmetric cone flare configuration.

Recently, a frequency domain-based resolvent analysis has been introduced to investigate the amplification properties of different supersonic/hypersonic flow phenomena, such as boundary layer instabilities over flat plates, shock/boundary layer interactions over compression ramps and double wedges, and local centrifugal (Görtler-type) instability on axisymmetric geometries with concave flares.^{33–37} This technique yields a nonmodal growth (optimal gain) that characterizes flow response subject to external forcing, and is directly related to the noise amplifier nature.³⁸ Different from the LST and the PSE, the assumption of parallel flow is not required in the resolvent analysis, and the base flow considered could be of higher dimension. As highlighted in Bugeat *et al.*,³⁶ the optimal gain obtained from the resolvent analysis is a global quantity that accounts for the energy growth of perturbations over a given physical domain, and is influenced by the size of the computational domain. Its absolute value has no physical meaning. The objective of this study is to

revisit the Görtler instability developing over a concave wall using the resolvent analysis and investigate how the instability behaves subject to different geometric parameters and flow conditions in the high-speed flow regime.

Both the geometries of the concave wall and the flow conditions are pertinent to the generation of the Görtler instability; however, a few studies have summarized these conditions change to the instability parametrically, in particular from the perspective of global stability. For example, geometric factors are critical to accurately model the centrifugal force field.² The streamwise extent (or the arc length) D of the concave wall is a function of both the radius of curvature R and the turning angle θ , i.e., $D = f(R, \theta)$, as shown in Fig. 1. Bippes³⁹ proposed a dimensionless wavelength parameter Λ based on the Görtler number (i.e., $G \equiv Re\sqrt{\delta_x/R}$ as a function of Reynolds number Re , boundary layer length scale δ_x , and radius of curvature R) such that the maximum amplification over Λ equal a constant;⁴⁰ however, the original wavelength parameter is proposed for incompressible flow only. In this study, we aim to investigate the change in these geometric parameters on the stationary Görtler instability through parametric studies, together with the change in different flow conditions (i.e., the variation in Mach number, Reynolds number and wall temperature). The resolvent analysis is used to identify the most amplified spanwise wavenumber, while the LST is used to verify if the instability captured by the resolvent analysis belongs to convective-type or component-type nonmodalities. As defined in the literature,³⁶ the convective-type nonmodality arises from the advection of perturbations by the base flow (e.g., Görtler instability in this study, or Mack mode instability), while the component-type (or lift-up) nonmodality is caused by the transport of base flow momentum by the perturbation. A new wavelength parameter is proposed to predict the most unstable spanwise wavelength with the consideration of compressibility. Finally, a three-dimensional (3D) numerical simulation with steady forcing is conducted to validate the findings in the stability analysis.

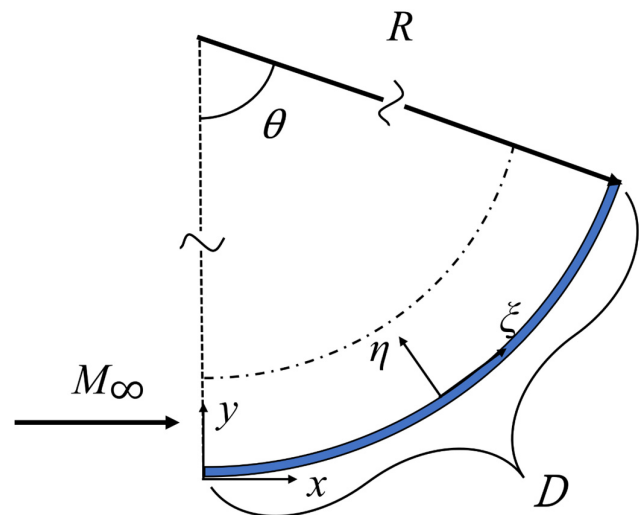


FIG. 1. Schematic of the two-dimensional (2D) concave wall configuration. The region covered within the dot-dashed line and the concave plate is the computational domain.

II. GEOMETRY OF CONCAVE WALL AND FLOW

The geometry considered in this study is a concave wall with constant curvature (see Fig. 1). A Cartesian coordinate system is constructed with the origin at the leading edge, the x direction along the freestream, the z direction along the leading edge, and the y direction satisfying the right-hand rule. A curvilinear coordinate system is also defined, where ξ is the distance along the model surface measured from the leading edge and η is the wall-normal distance from the model surface. The two coordinates share the same z direction. The corresponding Lamé coefficients are $h_1 = 1 + \kappa\eta$ and $h_2 = h_3 = 1$, where $\kappa = -1/R$ is the streamwise curvature.

The concave wall in the baseline case has a radius of curvature $R = 1600$ mm, a turning angle of $\theta = 10.62^\circ$, and an arc length of $D = 296.6$ mm. The baseline freestream conditions have a Mach number of $M_\infty = 6.5$, a static temperature of $T_\infty = 53$ K and a unit Reynolds number of $Re_\infty = 9.0 \times 10^6 \text{ m}^{-1}$, as summarized in Table I. The above geometric and flow parameters are varied to investigate their effects on the Görtler instability. For different cases, the region of interest is $\xi \in [1/6D, 5/6D]$. In the baseline case, this corresponds to $x \in [49.4, 246.2]$ mm ($\xi \in [49.4, 247.2]$ mm), $Re \equiv \sqrt{Re_\infty x} \in [667, 1489]$, and $G \equiv Re\sqrt{\delta_x/R} \in [4.5, 15.1]$, where $\delta_x = \sqrt{x/Re_\infty}$. According to Hall²⁰ and Bottaro and Luchini,²⁵ local stability analysis is applicable at downstream locations.

III. COMPUTATIONAL DETAILS

A. Governing equations

The governing equations are the compressible Navier–Stokes (NS) equations written in the following conservation form:

$$\frac{\partial \mathbf{U}}{\partial t} + \frac{\partial (\mathbf{F} - \mathbf{F}_v)}{\partial x} + \frac{\partial (\mathbf{G} - \mathbf{G}_v)}{\partial y} + \frac{\partial (\mathbf{H} - \mathbf{H}_v)}{\partial z} = 0, \quad (1)$$

where $\mathbf{U} = [\rho, \rho u, \rho v, \rho w, \rho e]^T$ is the vector of conservative variables and the vectors of flux are given as follows:

$$\mathbf{F} = \begin{bmatrix} \rho u \\ \rho u^2 + p \\ \rho uv \\ \rho uw \\ (\rho e + p)u \end{bmatrix}, \quad \mathbf{F}_v = \begin{bmatrix} 0 \\ \tau_{xx} \\ \tau_{xy} \\ \tau_{xz} \\ u\tau_{xx} + v\tau_{xy} + w\tau_{xz} - q_x \end{bmatrix}. \quad (2)$$

Vectors \mathbf{G} , \mathbf{G}_v , \mathbf{H} , and \mathbf{H}_v are expressed analogously. In these expressions, ρ is the density, u , v , and w are the velocities in the x , y , and z directions, respectively, p is the pressure, and e is the total energy per unit mass. The viscous stress tensors τ are evaluated according to the Newtonian fluid and the Stokes hypothesis, where the dynamic viscosity is calculated using Sutherland's law. The heat flux vector \mathbf{q} is modeled based on Fourier's law, where the coefficient of thermal conductivity k is obtained by assuming a constant Prandtl number of

TABLE I. Geometric and flow parameters for the baseline case.

R (mm)	θ	M_∞	Re_∞ (m^{-1})	T_∞ (K)
1600	10.62°	6.5	9.0×10^6	53

0.72. A calorically perfect gas is assumed with a constant specific heat ratio of 1.4.

The flow variables are normalized with the corresponding free-stream parameters except that p is nondimensionalized by $\rho_\infty u_\infty^2$. The characteristic length L is fixed at 1 mm.

B. Base-flow solver

An in-house multiblock parallel finite-volume solver called PHAROS^{41,42} is used to conduct the numerical simulation. In this solver, the inviscid fluxes are evaluated using the modified Steger–Warming scheme.⁴³ A second-order central difference is used to calculate the viscous fluxes. The second-order MUSCL scheme with the van Leer slope limiter⁴⁴ is implemented for the reconstruction of variables. For pseudotime stepping, an implicit line relaxation method⁴⁵ is applied. The freestream conditions are specified on the left and upper boundaries of the computational domain (see Fig. 1). A simple extrapolation is used on the right boundary. The wall is assumed to be isothermal and no-slip. Grid convergence is demonstrated in Appendix, and 600×300 grids in 2D simulation is sufficient for the present study.

C. Linear stability analysis

Under the local parallel flow assumption, the instantaneous flow is decomposed into a one-dimensional (1D) steady solution (denoted by an overbar) and an unsteady perturbation (denoted by a prime) as follows:

$$\mathbf{U}(\xi, \eta, z, t) = \bar{\mathbf{U}}_{1-D}(\eta) + \mathbf{U}'(\xi, \eta, z, t). \quad (3)$$

The governing equation of \mathbf{U}' is evaluated by substituting Eq. (3) into Eq. (1) and neglecting the higher order terms. \mathbf{U}' is further assumed to be in the following normal-mode form for spatial analysis:

$$\mathbf{U}'(\xi, \eta, z, t) = \hat{\mathbf{U}}_{1-D}(\eta) \exp[i(\alpha_r + i\alpha_i)\xi + i\beta z - i\omega t] + c.c., \quad (4)$$

where $\hat{\mathbf{U}}_{1-D}(\eta)$ is the 1D eigenfunction in the wall-normal direction, α_r is the real streamwise wavenumber, α_i is the spatial growth rate, β is the spanwise wavenumber, ω is the angular frequency, and $c.c.$ is the complex conjugate. Substituting Eq. (4) into the linearized Eq. (1) leads to an eigenvalue problem as follows:

$$\bar{\mathbf{A}}_{1-D} \hat{\mathbf{U}}_{1-D} = (\alpha_r + i\alpha_i) \hat{\mathbf{U}}_{1-D}, \quad (5)$$

where $\bar{\mathbf{A}}_{1-D}$ is the 1D Jacobian matrix consisting of inviscid and viscous fluxes and can be found in the literature.^{15,46} With the given ω and β , a C++ library Eigen⁴⁷ is used to solve this eigenvalue problem. The unstable mode is determined if the growth rate $\alpha_i < 0$. The boundary conditions in the LST are consistent with those for the base flow. Figure 2 presents a comparison between the results obtained from the present LST solver and the literature for both incompressible²⁶ and compressible boundary layers.¹² Figure 3 demonstrates the typical disturbance profiles of streamwise velocity and temperature for cases of $M = 1.5, 3.0$, and 4.5 , computed using compressible Blasius boundary layers.¹² The overall good agreement between the presented profiles and the literature verifies the use of the LST solver in this study.

D. Resolvent analysis

Global resolvent analysis (GRA) investigates the response of a 2D globally stable base flow to an external forcing \mathbf{f}' that is small in

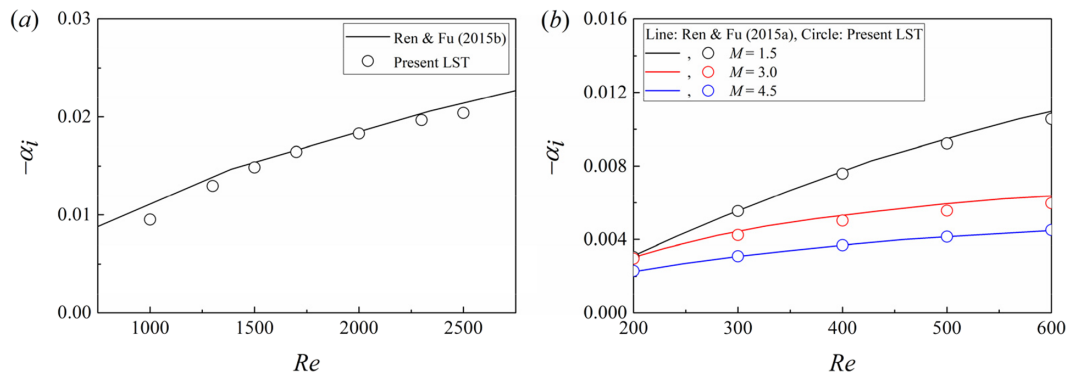


FIG. 2. Growth rate of the most unstable Görtler mode as a function of the Reynolds number computed by the present LST solver for a) an incompressible flow case²⁶ with $\omega/Re = 1.0 \times 10^{-5}$, $\beta/Re = 2.5 \times 10^{-4}$ and $\kappa/Re = -1.0 \times 10^{-6}$, and b) compressible flow cases¹² at $M = 1.5, 3.0$, and 4.5 with $\omega/Re = 0$, $\beta/Re = 2.0 \times 10^{-3}$, and $\kappa/Re = -1.0 \times 10^{-6}$.

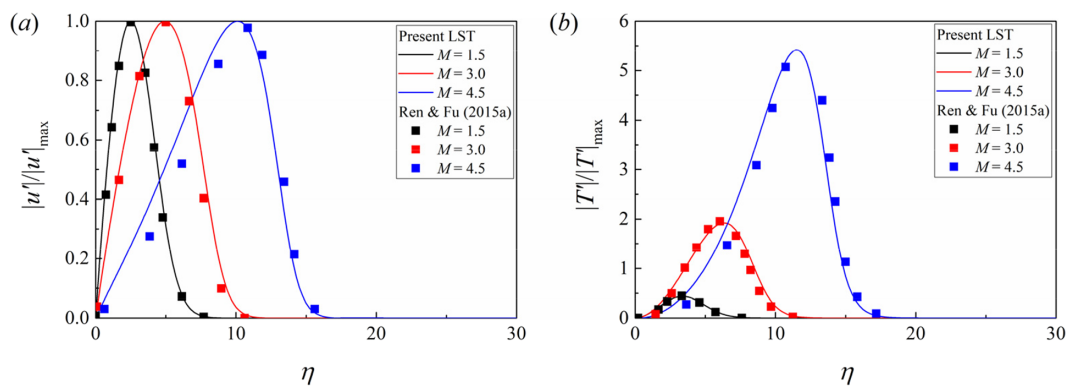


FIG. 3. Disturbance profiles of normalized (a) $|u'|$ and (b) $|T'|$ for the most unstable Görtler mode in compressible flow cases¹² at $M = 1.5, 3.0$, and 4.5 . $Re = 400$, $\omega/Re = 0$, $\beta/Re = 1.0 \times 10^{-3}$, and $\kappa/Re = -1.0 \times 10^{-6}$.

amplitude. Different from the linearization in Sec. III C, the vector \mathbf{U} in this study is decomposed into a 2D base flow with an unsteady perturbation term,

$$\mathbf{U}(x, y, z, t) = \bar{\mathbf{U}}_{2-D}(x, y) + \mathbf{U}'(x, y, z, t). \quad (6)$$

The linearized NS equations are then given in the following semi-discrete form,

$$\frac{\partial \mathbf{U}'}{\partial t} = \bar{\mathbf{A}}_{2-D} \mathbf{U}' + \bar{\mathbf{B}} \mathbf{f}', \quad (7)$$

where $\bar{\mathbf{A}}_{2-D}$ is the global Jacobian matrix obtained through the linearization of the 2D discretized compressible NS equations and can be found in Hao *et al.*⁴⁸ The matrix $\bar{\mathbf{B}}$ confines the forcing to a localized region, where different ranges of x/L (or ξ/L) and y/L (or η/L) can be specified. For instance, to represent upstream disturbance, the forcing in this study is localized at approximately one-sixth of D for the whole y -plane, as illustrated in Sec. IV A later. The submatrices of matrix $\bar{\mathbf{B}}$ are set to the identity matrix in cells at the forcing location and zero elsewhere. The forcing \mathbf{f}' is formulated as follows:

$$\mathbf{f}'(x, y, z, t) = \hat{\mathbf{f}}(x, y) \exp(i\beta z - i\omega t). \quad (8)$$

As time goes to infinity (i.e., the long-time solution), all the perturbations initially introduced on a globally stable flow decay to zero. Therefore, \mathbf{U}' takes the same form as \mathbf{f}' , which is given by

$$\mathbf{U}'(x, y, z, t) = \hat{\mathbf{U}}_{2-D}(x, y) \exp(i\beta z - i\omega t). \quad (9)$$

Substituting Eq. (9) and Eq. (8) into Eq. (7) yields the following relation:

$$\hat{\mathbf{U}}_{2-D} = \bar{\mathbf{R}} \bar{\mathbf{B}} \hat{\mathbf{f}}, \quad \bar{\mathbf{R}} = (-i\omega \mathbf{I} - \bar{\mathbf{A}}_{2-D})^{-1}, \quad (10)$$

where $\bar{\mathbf{R}}$ is the resolvent matrix depends on the dimension of $\bar{\mathbf{A}}_{2-D}$ and \mathbf{I} is the identity matrix.

The maximized energy amplification (or optimal gain σ) with the given forcing and response pair is defined by

$$\sigma^2(\beta, \omega) = \max_{\hat{\mathbf{f}}} \frac{\|\hat{\mathbf{U}}_{2-D}\|_e}{\|\bar{\mathbf{B}} \hat{\mathbf{f}}\|_e}. \quad (11)$$

The energy norm is defined based on the Chu energy.^{49,50} Referring to the literature,^{33,36,51} the optimization problem in Eq. (11) can be converted into an eigenvalue problem as follows:

$$\bar{\mathbf{B}}^\dagger \bar{\mathbf{M}}^{-1} \bar{\mathbf{R}}^\dagger \bar{\mathbf{M}} \bar{\mathbf{R}} \bar{\mathbf{B}} \hat{\mathbf{f}} = \sigma^2 \hat{\mathbf{f}}, \quad (12)$$

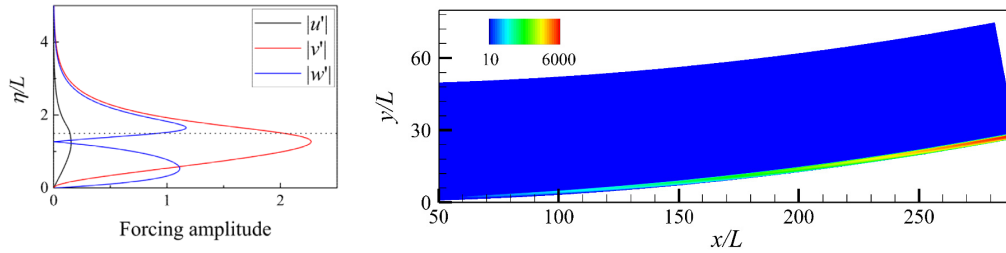


FIG. 4. The most amplified optimal forcing at $\xi/L = 48.7$ (left) and response (right) at $\beta = 2.3$ and $\omega = 0$ for the baseline case. Horizontal dotted line denotes the boundary layer edge at 99% of the free-stream streamwise velocity. Only the $|u'|$ contour is shown for the optimal response.

where the superscript \dagger represents the complex conjugate and $\bar{\mathbf{M}}$ is the weight matrix for calculating the Chu energy and has the same dimension as $\bar{\mathbf{R}}$.³⁶ Finally, the eigenvalue problem is solved using ARPACK⁵² in the regular mode. The inverse of the matrix and its conjugate transpose are obtained using the lower-upper decomposition implemented in Super-LU.⁵³ The optimal gain is denoted by the largest eigenvalue, while the optimal forcing is denoted by the corresponding eigenfunction. The optimal response can be obtained through Eq. (10). The boundary conditions in resolvent analysis are consistent with those for the base flow.

Figure 4 shows a typical result from the resolvent analysis for the most amplified optimal forcing (at $\xi/L = 48.7$) and response pairs at $\beta = 2.3$ and $\omega = 0$ for a baseline case (see Table I). The forcing is in the type of counter-rotating streamwise vortices (i.e., $|u'| \ll |v'|$ and $|u'| \ll |w'|$) while the responses are streamwise streaks (i.e., $|u'| \gg |v'|$ and $|u'| \gg |w'|$).

IV. RESULTS

A. Notes on the LST and the resolvent analysis

This subsection considers the sensitivity of the stability results to different downstream profiles in the LST. The effects of different positions of the forcing on the instability in the resolvent analysis for the baseline case are then examined. The N factor calculations for both the LST and the resolvent analysis are introduced at last, and these representations will be used in the remaining parts of the section.

The spatial growth rate from the LST at different specified ξ/L positions for the baseline case is presented in Fig. 5. Multiple Görtler modes would be obtained in the LST as reported in the literature,⁴⁶ however, we are only interested in the most unstable mode in this study. The most unstable β stays the same within $\xi \in [1/3D, 2/3D]$ (or $\xi/L \in [98.0, 195.5]$), and a slight shift with 0.1 is observed further downstream. The growth rate is also insensitive to streamwise location changes. Therefore, it is appropriate to select the 1D base flow profile within the above region of interest for the LST.

The sensitivity of the localized forcing region in the resolvent analysis is examined with different streamwise positions and wall-normal ranges. Figure 6(a) shows the optimal gain obtained in which the forcing is specified at different ξ/L positions for the entire η plane. Note that ξ/L ranges from 0 to 296.6 for the baseline case. The optimal gains over the considered range of spanwise wavenumber are elevated as the forcing location moves upstream. The largest optimal gain is achieved if the entire region between $\xi/L = 48.7$ and 243.7 is forced. However, the most unstable optimal gains almost overlap at $\beta_{\max} = 2.3$, except for a marginal difference with the forcing localized

far downstream (i.e., $\xi/L > 195.0$). In other words, the forcing position can be arbitrary set within $\xi/L = 48.7\text{--}195.0$ (i.e., approximately one-sixth of D to four-sixth of D), with minimal variation observed in the behavior of the optimal gain. Although not shown here, the optimal forcings and responses are in the same form as those shown in Fig. 4. In the remainders, the forcing of the resolvent analysis is localized at $\xi/L = 48.7$ (i.e., around one-sixth of D) unless otherwise specified.

Figure 6(b) shows the optimal gain obtained with forcing at the specified ξ/L position in which the regions covered at the wall-normal directions change, starting from the wall at $\eta/L = 0$. The most unstable spanwise wavenumber β_{\max} shifts to a larger value if the forcing covers a larger region in the wall-normal direction below the boundary layer edge (i.e., ranges of $\beta_{\max} = 1.7\text{--}2.3$ are recorded). For the case of forcing covering the region above the boundary layer edge (i.e., $(\eta/L)_{\max} > 3.0$, β_{\max} remains unchanged), the forcing introduced outside the boundary layer has no effect on the stability analysis. For convenience, the input forcing in the resolvent analysis is implemented at the entire η plane unless otherwise specified.

The corresponding N factor for the resolvent analysis (N_{GRA}) and the LST (N_{LST}) is computed based on the relation below:

$$N_{\text{GRA}} = \frac{1}{2} \ln \left(\frac{E_{\text{Chu}}}{E_{\text{Chu},0}} \right), \quad (13)$$

$$N_{\text{LST}} = \int_{\xi_0}^{\xi} -\alpha_i d\xi, \quad (14)$$

where E_{Chu} is the integrated Chu's energy across the ξ -direction^{36,49,50} and $E_{\text{Chu},0}$ is the integrated Chu's energy at the position right after

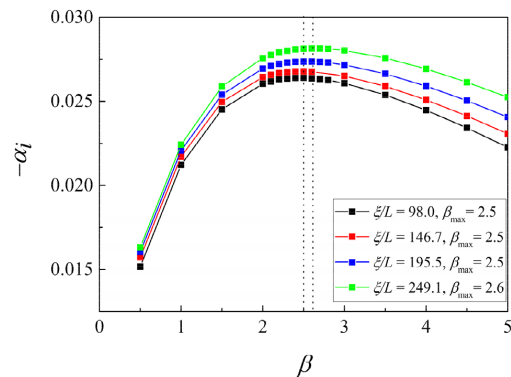


FIG. 5. Spatial growth rate from the LST of the baseline case at different ξ/L positions. $\omega = 0$ is fixed. Vertical dotted lines denote the ranges of β_{\max} recorded.

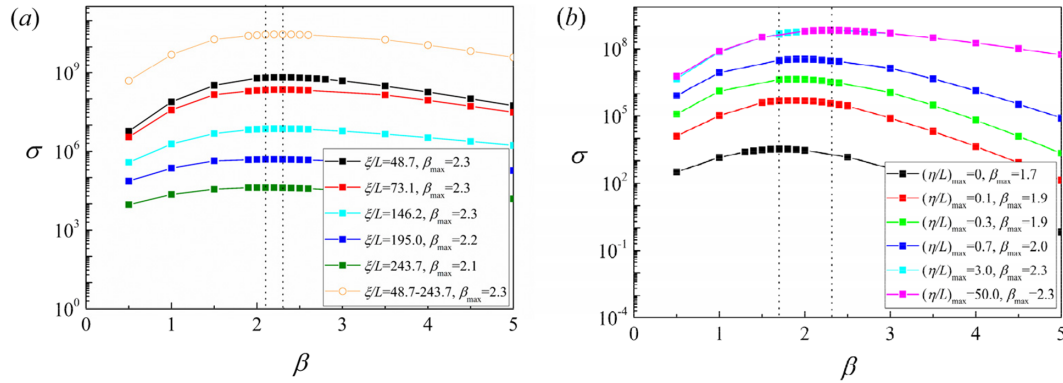


FIG. 6. Optimal gain from the resolvent analysis of the baseline case at (a) different ξ/L positions of forcing and (b) different wall-normal forcing ranges at $\xi/L = 49.7$. For (a), forcing is implemented for the entire η plane with $\omega = 0$. The line with the empty circle pattern denotes the case with forcing at the specified streamwise ranges; for (b), forcing with $\omega = 0$ is implemented from $\eta/L = 0$ at the wall-normal direction up to the corresponding $(\eta/L)_{\max}$, and $(\eta/L)_{\max} = 50.0$ represents the forcing at the entire η plane, while $(\eta/L)_{\max} = 0$ represents the forcing at the wall. Vertical dotted lines denote the ranges of β_{\max} recorded.

the forcing is implemented. The formulations of the corresponding N factor in Eqs. (13) and (14) follow the definition reported by van Ingen.⁵⁴

B. Effect of changes in geometric and flow conditions

In this section, the effects of changes in geometric factors, including R and θ , on the Görtler instability, are demonstrated first, followed by those of changes in flow conditions (i.e., Re_∞ , T_w/T_∞ , and M). Finally, a new dimensionless wavelength parameter for compressible flow is proposed.

The effect of varying the radius of curvature on the Görtler instability is investigated. Four different radii of curvature are considered: $R = 500$ mm (R0.5), 1000 mm (R1.0), 1600 mm (R1.6), and 2000 mm (R2.0). Figure 7(a) shows the optimal gain and growth rate under the change in radius of curvature R . Since D varies with R , the forcing position test was conducted for other R cases, similar to Fig. 6 on R1.6 under Sec. IV A, which is not presented here due to redundancy.

Based on these tests, the forcing position in the resolvent analysis is set to one-sixth of D (e.g., $\xi/L = 48.7$ for the R1.6 case). Overall, the most unstable β shifts to a smaller value as R increases (e.g., $\beta_{\max} = 3.6$ to 2.1 from R0.5 to R2.0 in the resolvent analysis). The same trend is observed in the LST results, which agree well the resolvent analysis results at relatively large spanwise wavenumbers. Discrepancies can be seen as β approaches zero. This is because high-order curvature terms are neglected in the LST.³ The optimal gain decreases as the radius decreased, which does not indicate a stabilization effect but results from the decreasing computational domain. As mentioned in the work of Bugeat *et al.*,³⁶ the optimal gain is dependent on both the growth rate of the instability and the length (or computational domain) over which the perturbation grows. The behavior of the optimal gain as a function of β is deemed more significant than the absolute optimal gain.⁵¹ Figure 7(b) shows the corresponding N factors deduced from both the resolvent analysis and the LST for the specified β . The maximum N factor obtained from the resolvent analysis is consistently higher than that in the LST (i.e., $N = 6.4$ in the resolvent

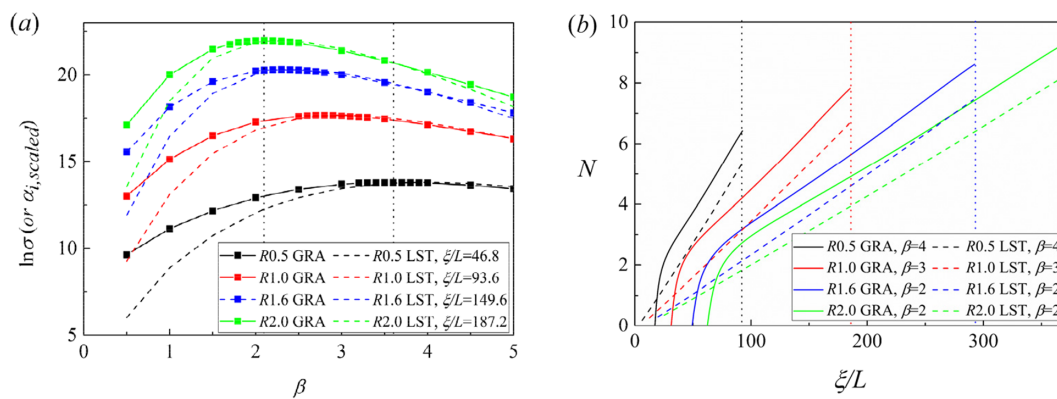


FIG. 7. (a) Optimal gain from the resolvent analysis and the spatial growth rate [i.e., α_i , scaled = $\alpha_i/\alpha_{i,\max} \times (\ln \sigma)_{\max}$] from the LST under the change in radius of curvature with $\omega = 0$. The corresponding ξ/L positions for the LST are specified. Vertical dotted lines show the range of β_{\max} recorded by the resolvent analysis. (b) The corresponding N factor based on the resolvent analysis and the LST along the ξ -direction at specified β . Vertical dotted lines with the corresponding colors denote the end of the ξ -domain for each R case. $\theta = 10.62^\circ$, $M_\infty = 6.5$, $Re_\infty = 9.0 \times 10^6 \text{ m}^{-1}$, and $T_w/T_\infty = 8.0$.

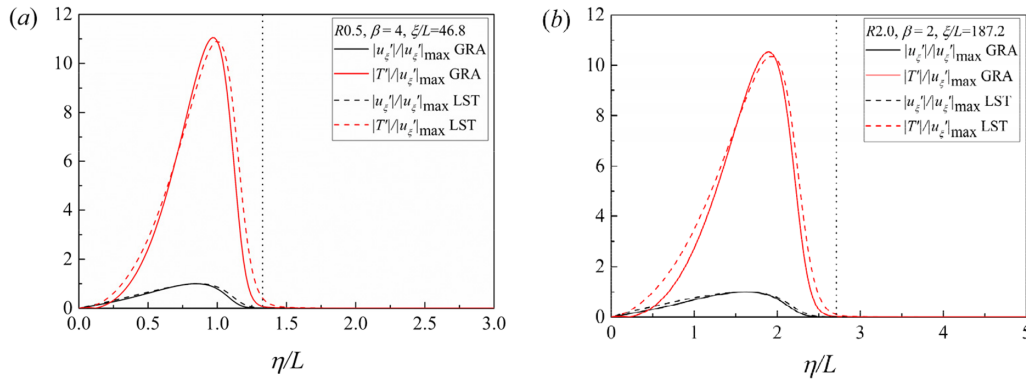


FIG. 8. Disturbance profiles of $|u'_\xi|$ and $|T'|$ normalized with maximum $|u'_\xi|$ from the resolvent analysis and the LST along the wall-normal direction for the (a) R0.5 and (b) R2.0 cases. In GRA, $|u'_\xi|$ is obtained through the coordinate transformation. The corresponding β and ξ/L positions (approximately one-half of the corresponding D) are specified. The vertical dotted line denotes the boundary layer edge. $\theta = 10.62^\circ$, $M_\infty = 6.5$, $Re_\infty = 9.0 \times 10^6 \text{ m}^{-1}$, and $T_w/T_\infty = 8.0$.

analysis and $N=5.3$ in the LST for R0.5). However, the identical slopes recorded by both methods in the far downstream region indicate that the instability is of the same nature. Recall that the LST captures local modal growth, while the optimal gain in resolvent analysis is global in nature, the discrepancies between N_{GRA} and N_{LST} across ξ suggests the existence of nonmodal (transient) growth, specifically the lift-up mechanism, immediately downstream of the forcing. This lift-up mechanism is typical observed when the optimal forcing takes the form of counterrotating streamwise vortex [Fig. 4(a)], initiating the transport of streamwise momentum of the base flow.^{36,55} The steeper slope at the smaller radius of curvature in Fig. 7(b) is reminiscent of the fact that the decrease in radius of curvature destabilizes the Görtler instability. This trend of destabilization has been reported in previous literature,^{2,3} and recent experiments on both incompressible⁵⁶ and compressible boundary layers⁵⁷ support this argument. The destabilization of Görtler instability can be attributed to the excitation of centrifugal force as the wall curvature increases. In contrast, the Görtler instability is always absent in the case of a flat plate (i.e., the wall curvature is zero).

Figure 8 shows a good agreement between the disturbance profiles at the specified ξ/L (subscript ξ) obtained by the two methods, further confirming that the existing instability in this study is solely of the Görtler type. According to Song *et al.*,¹⁵ the temperature perturbation is approximately ten times larger than the streamwise velocity perturbation under such baseline flow conditions, which is emblematic of the Görtler instability. The primary (the most unstable) Görtler instability recorded in this study is the trapped-layer mode, as its disturbances detach from the wall.¹²

Next, the effect of the change in turning angle θ at fixed R1.6 on the Görtler instability is examined. This is achieved by individually varying θ (i.e., 5.36° , 10.62° , and 14.04°), where the arc length D differs for each θ case. The corresponding optimal gains, growth rates, and N factors obtained from the resolvent analysis and LST are shown in Fig. 9. Note that the forcing in the resolvent analysis is specified at $\xi/L = 48.7$. The spanwise wavenumber and the growth rate of the most amplified instability remain largely unchanged, which indicates that the Görtler instability is insensitive to the change in θ . Similarly, the constant discrepancies between N_{GRA} and N_{LST} across ξ , with a

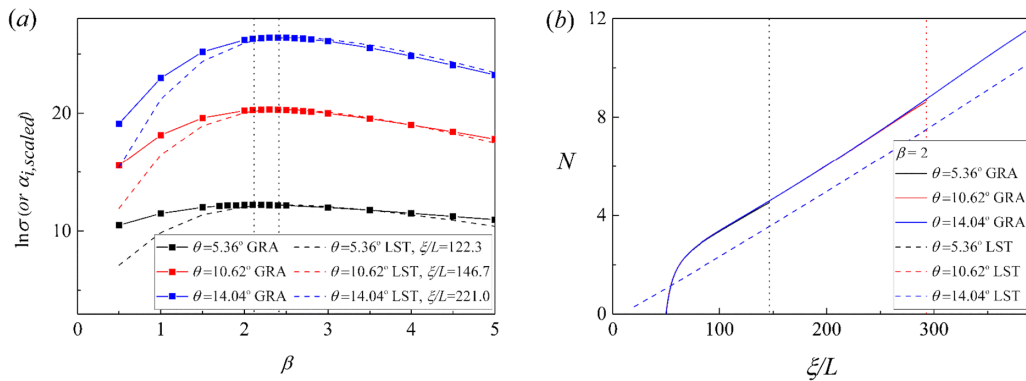


FIG. 9. (a) Optimal gain from the resolvent analysis and the spatial growth rate (i.e., $\alpha_{i,\text{scaled}} = \alpha_i/\alpha_{i,\text{max}} \times (\ln \sigma)_{\text{max}}$) from the LST under the change in turning angle with $\omega = 0$. The corresponding ξ/L positions for the LST are specified. Vertical dotted lines show the range of β_{max} recorded by the resolvent analysis. (b) The corresponding N factor based on the resolvent analysis and the LST along the ξ -direction at specified β . Vertical dotted lines with the corresponding colors denote the end of the ξ -domain for each θ case. $R = 1600 \text{ mm}$, $M_\infty = 6.5$, $Re_\infty = 9.0 \times 10^6 \text{ m}^{-1}$, and $T_w/T_\infty = 8.0$.

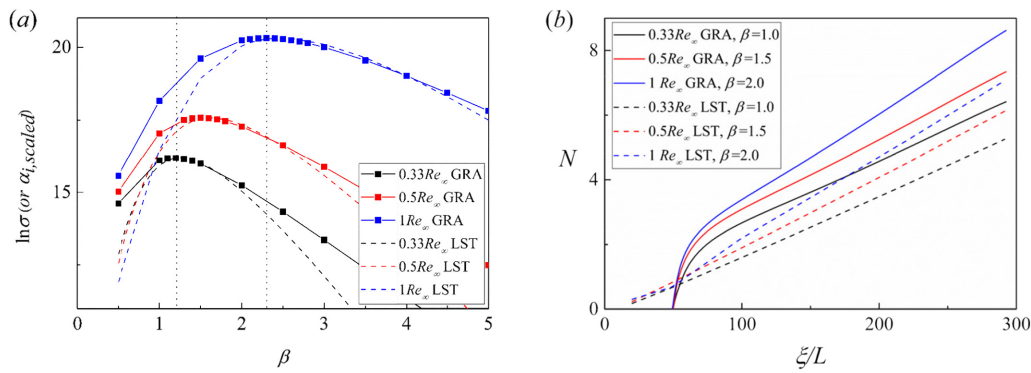


FIG. 10. (a) Optimal gain from the resolvent analysis and the spatial growth rate [i.e., $\alpha_{i, \text{scaled}} = \alpha_i / \alpha_{i, \text{max}} \times (\ln \sigma)_{\text{max}}$] from the LST under the change in Reynolds number with $\omega = 0$. For the LST, $\xi/L = 146.7$ is specified. Vertical dotted lines denote the range of β_{max} recorded by the resolvent analysis. (b) The corresponding N factor based on the resolvent analysis and the LST along the ξ -direction at specified β . $R = 1600$ mm, $\theta = 10.62^\circ$, $M_\infty = 6.5$, and $T_w/T_\infty = 8.0$.

difference of approximately $N = 1$ at $\xi/L > 100$, signify the presence of lift-up nonmodality. Again, the optimal gain is increased as the computational domain is enlarged. The minimal impact on the Görtler instability can be attributed to the negligible change in centrifugal forces among the various θ cases, as increasing θ only extends the concave surface length while leaving the local wall curvature unchanged. Therefore, the boundary layer thickness is roughly constant among all θ cases, i.e., approximately $\eta/L = 2$ at half of D , indicating that base flow's self-similar properties hold and are independent of θ .

The impact of flow conditions on the Görtler instability is also investigated. Figure 10 shows the optimal gains, growth rates, and N factors computed for three different Re_∞ (i.e., $0.33 Re_\infty$, $0.5 Re_\infty$, and $1 Re_\infty$, where $0.5 Re_\infty$ denotes decreasing the Reynolds number by a factor of 0.5). The results indicate that decreasing the Reynolds number leads to flow stabilization, with a shift to lower β_{max} (e.g., $\beta_{\text{max}} = 1.2$ for $0.33 Re$ in the resolvent analysis). This trend is also observed in the LST analysis. A similar observation regarding the difference between N_{GRA} and N_{LST} (with a magnitude of approximately $N = 1$ at $\xi/L > 100$) was recorded, identifying the contribution from the constant transient growth (lift-up effect) downstream. It is indicated that

the wavelength of the Görtler instability scales with the boundary-layer thickness. In boundary layer theory, the boundary layer thickness is known to exhibit an inverse relationship with the Reynolds number (or density). For instance, the boundary layer represented by the velocity profile in $0.33 Re$ case thickens by a factor of 1.75 compared to the $1 Re_\infty$ case. As the boundary layer thickness decreases, the convective instability (i.e., the Görtler instability) becomes destabilized.

The impact of wall cooling is examined by varying the wall temperature to total temperature ratio T_w/T_∞ . The baseline condition with $T_w/T_\infty = 8.0$ is close to an adiabatic wall condition (i.e., $T_w/T_\infty = 8.9$). Figure 11 shows the optimal gains, growth rates, and N factors under the change of T_w/T_∞ (i.e., $T_w/T_\infty = 2.4, 4.3$, and 8.0). Both the optimal gain and the growth rate of the most amplified Görtler instability increase due to wall cooling, while the corresponding β shifts to a larger value (e.g., $\beta_{\text{max}} = 3.4$ at $T_w/T_\infty = 2.4$) in accordance with the decreasing boundary-layer thickness (i.e., thinning by half at $T_w/T_\infty = 2.4$ compared with $T_w/T_\infty = 8.0$, not shown here). The constant disparity (around $N = 1$ at $\xi/L > 100$) between N_{GRA} and N_{LST} across ξ again identifies the component-type nonmodality. The destabilization effect at a thinner boundary layer is consistent with the literature regarding the wall cooling effects on the

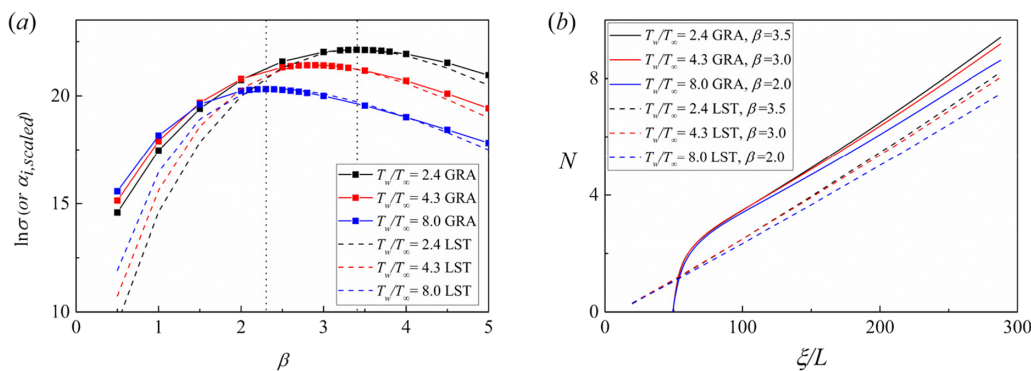


FIG. 11. (a) Optimal gain from the resolvent analysis and the spatial growth rate [i.e., $\alpha_{i, \text{scaled}} = \alpha_i / \alpha_{i, \text{max}} \times (\ln \sigma)_{\text{max}}$] from the LST under the change in T_w/T_∞ with $\omega = 0$. For the LST, $\xi/L = 146.7$ is specified. Vertical dotted lines denote the range of β_{max} recorded by the resolvent analysis. (b) The corresponding N factor based on the resolvent analysis and the LST along the ξ -direction at specified β . $R = 1600$ mm, $\theta = 10.62^\circ$, $M_\infty = 6.5$, and $Re_\infty = 9.0 \times 10^6 \text{ m}^{-1}$.

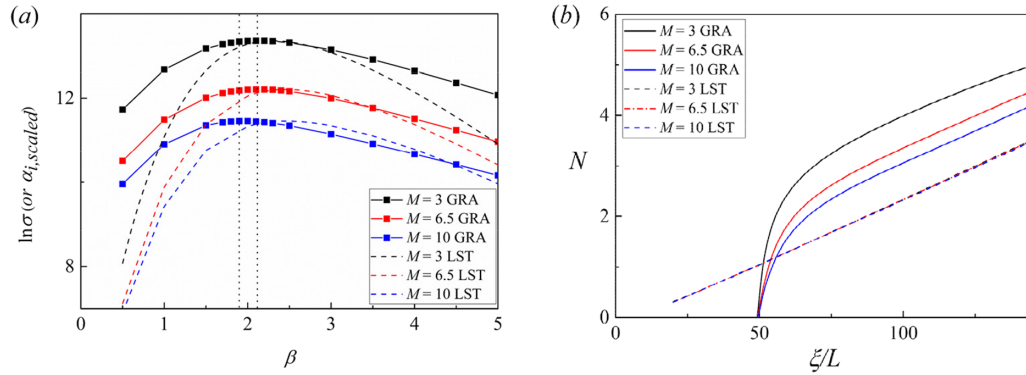


FIG. 12. (a) Optimal gain (normalized to maintain the unit maximum value) from the resolvent analysis and the spatial growth rate (normalized to maintain the unit maximum value) from the LST on the change in M with $\omega = 0$. For the LST, $\xi/L = 122.3$ is specified. Vertical dotted lines denote the range of β_{max} recorded by the resolvent analysis. (b) The corresponding N factor based on the resolvent analysis and the LST along the x -direction. $\beta = 2$ is specified. $R = 1600$ mm, $\theta = 5.36^\circ$, $Re_\infty = 9.0 \times 10^6$ m $^{-1}$, and $T_w/T_\infty = 8.0$.

convective instability (e.g., Görtler or Mack mode instability) in compressible boundary layer.^{28,58}

To investigate the change in the Mach number to the Görtler instability, the baseline turning angle θ is fixed at 5.36° to prevent any flow separation at high turning angles. The total arc length D is 149.7 mm. The region of interest is $\xi/L \in [50, 130]$ and G (based on δ_x) $\in [4.6, 9.4]$ in this case.

Figure 12 shows the optimal gains, spatial growth rates, and N factors for different values of M (i.e., $M = 3, 6.5$, and 10). The spanwise wavenumber and the growth rate of the most amplified Görtler mode remain largely unchanged for the considered range of Mach number. However, the optimal gain and the N factor from the resolvent analysis decrease as M is increased, which indicates that the Mach number effect only manifests itself in the transient growth of streamwise vortices. In a similar parametric study by Spall and Malik²⁸ using compressible boundary layer equations in an adiabatic wall, they observed a stabilization in the local growth rate with increasing Mach number. This disparity could be attributed to the difference in boundary layer profiles computed in numerical simulation and that using the compressible boundary layer equations. Moreover, this study neglects the receptivity of the Görtler vortices to freestream vortical disturbance

(FSVD). Previous work by Viaro and Ricco²³ has demonstrated that in the presence of FSVD, the maximum streamwise velocity perturbation of Görtler vortices decreases downstream as the Mach number increases.

Boundary layer thickness manifested in velocity profile is closely associated with the strength of flow instability and its wavelength selection. In high-speed boundary layer flow over a concave plate, it is conventionally known that the boundary layer thickness scales parabolically with M . However, the velocity profiles along the model surface (at the specified ξ/L) in the wall-normal direction shown in Fig. 13(a) suggests that the boundary-layer thickness subject to an adverse pressure gradient is insensitive to the change in freestream Mach number. At $M_\infty = 3$, an inflection point can be seen near $\eta/L = 1.7$, which indicates that the boundary layer is about to separate from the wall. This insensitivity to the change of Mach number is observed in the temperature boundary layer thickness also [Fig. 13(b)].

In the early research on the Görtler instability in incompressible flow, a dimensionless wavelength parameter Λ is introduced in the literature^{3,39,40} to present the dimensional wavelength (or wavenumber) of the disturbance, which is constant in the streamwise direction as follows:

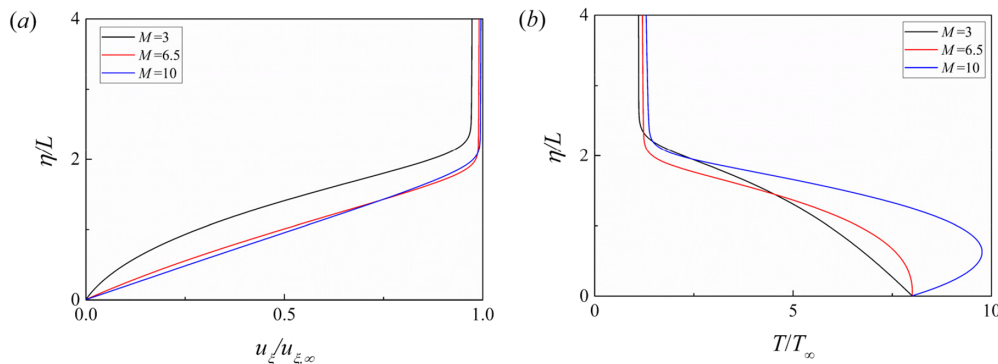


FIG. 13. (a) Mean velocity $u_\xi/u_{\xi, \infty}$ profiles and (b) mean temperature profiles along the wall-normal direction at $\xi/L = 122.3$ for each M case. $R = 1600$ mm, $\theta = 5.36^\circ$, $Re_\infty = 9.0 \times 10^6$ m $^{-1}$, and $T_w/T_\infty = 8.0$.

$$\Lambda = Re_{\infty} \lambda_z \sqrt{\frac{\lambda_z}{R}}, \quad (15)$$

where λ_z is the spanwise wavelength ($\lambda_z = 2\pi/\beta$). Originally, Λ considered the change in curvature (i.e., in terms of R) and that of the Reynolds number (i.e., in terms of Re_{∞}) in the expression such that the maximum amplification over Λ equal a constant. Based on the results of the parametric study in the previous paragraphs, the Görtler instability is found to be insensitive to changes in the turning angle θ and Mach number M , but sensitive to wall cooling effects in compressible flows. To account for these effects, Λ is modified by including T_w/T_{∞} as follows:

$$\Lambda_{\text{new}} = \sqrt{\frac{T_{\infty}}{T_w}} Re_{\infty} \lambda_z \sqrt{\frac{\lambda_z}{R}} = \sqrt{\frac{T_{\infty}}{T_w}} G \sqrt{\left(\frac{\lambda_z}{\delta_x}\right)^3}. \quad (16)$$

Figure 14 shows the change in the geometric and flow parameters discussed in the previous paragraphs against Λ_{new} and Λ instead of β . The most unstable Λ_{new} falls within 300–500. Since the effect of wall cooling is considered in the proposed expression, the most unstable mode is also confined in a narrow range of Λ_{new} , unlike the case against Λ [i.e., Fig. 14(c)].

Huang *et al.*⁷ conducted an experiment on a concave wall model to investigate the natural development of Görtler streaks in a Mach 6.5 wind tunnel at Peking University. The corresponding stagnation temperature is 435 K, and the unit Reynolds number is $5.5 \times 10^6 \text{ m}^{-1}$.

The adiabatic wall model has a radius of curvature of 800 mm. At $x=200 \text{ mm}$ where the linear streak is fully developed before the appearance of secondary instability (indicated by a typical mushroom-like structure), $\delta_x = \sqrt{x/Re_{\infty}} = 1.91 \times 10^{-4} \text{ m}$ and $G \equiv Re \sqrt{\delta_x/R} = 16.2$. The adiabatic wall temperature ratio (i.e., $T_w/T_{\infty} = 8.17$) is evaluated with a recovery factor of 0.85. Λ_{new} of the most dangerous Görtler instability is suggested to range from 300 to 500, corresponding to λ_z ranging from 2.69 to 3.78 mm in this case. The average wavelength measured in Huang *et al.*'s work⁷ is about 3.89 mm [nine packets within 35 mm in the spanwise direction in Fig. 4(f) in that study]. Despite the fact that the most unstable Görtler instability is not always confined at a constant Λ_{new} under the change of various parameters, a preliminary estimation of the most unstable spanwise wavelength from Λ_{new} is still beneficial to engineering design.

C. 3D numerical simulation

A 3D numerical simulation for the baseline case is conducted and compared with the resolvent analysis. A random forcing, formulated as follows,⁵⁹ is implemented until a steady state is reached,

$$w'_{j,k}/u_{\infty} = A_f(2r-1), \quad (17)$$

where j and k are the grid point indices in the η and z directions, respectively; A_f is the amplitude level of the disturbance; and r is a

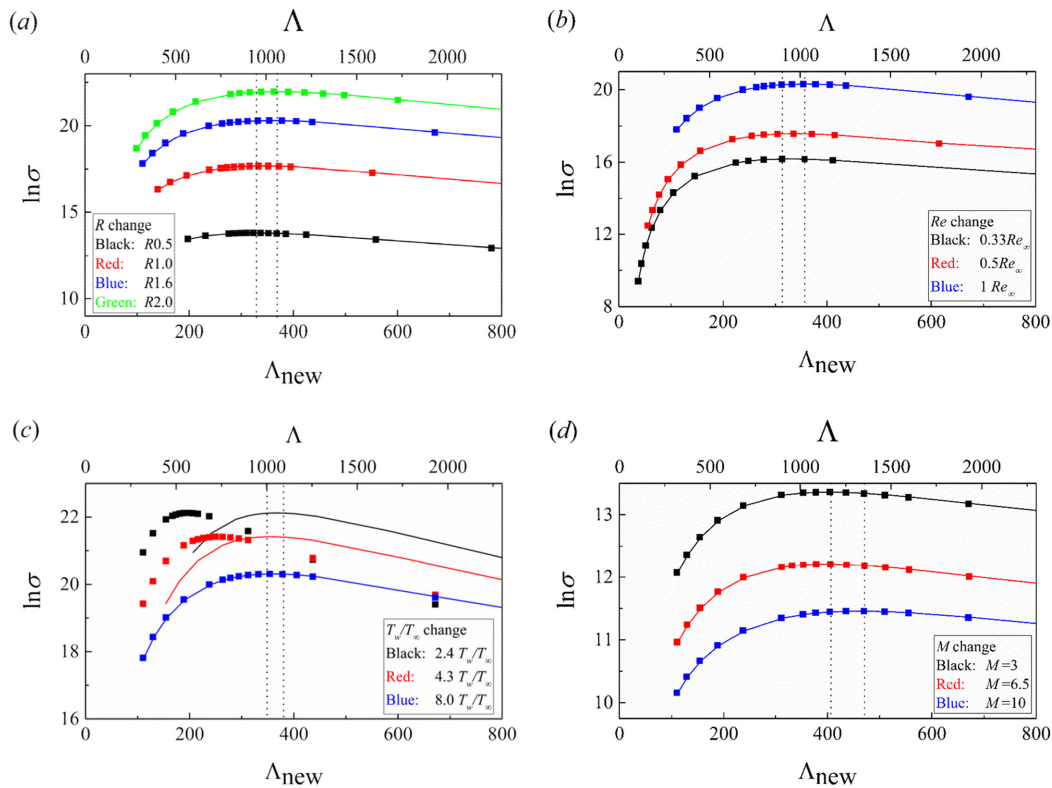


FIG. 14. Optimal gain vs Λ_{new} under changes in the (a) radius of curvature, (b) Reynolds number, (c) wall temperature ratio, and (d) Mach number. Solid lines represent the data along Λ_{new} (bottom x-axis) whereas solid squares represent the data along Λ (top x-axis). Vertical dotted lines denote the range of maximum Λ_{new} . $R=1600 \text{ mm}$, $\theta=10.62^\circ$, $M_{\infty}=6.5$, $Re_{\infty}=9.0 \times 10^6 \text{ m}^{-1}$, and $T_w/T_{\infty}=8.0$ are fixed unless the individual parameter change is specified in (a)–(d).

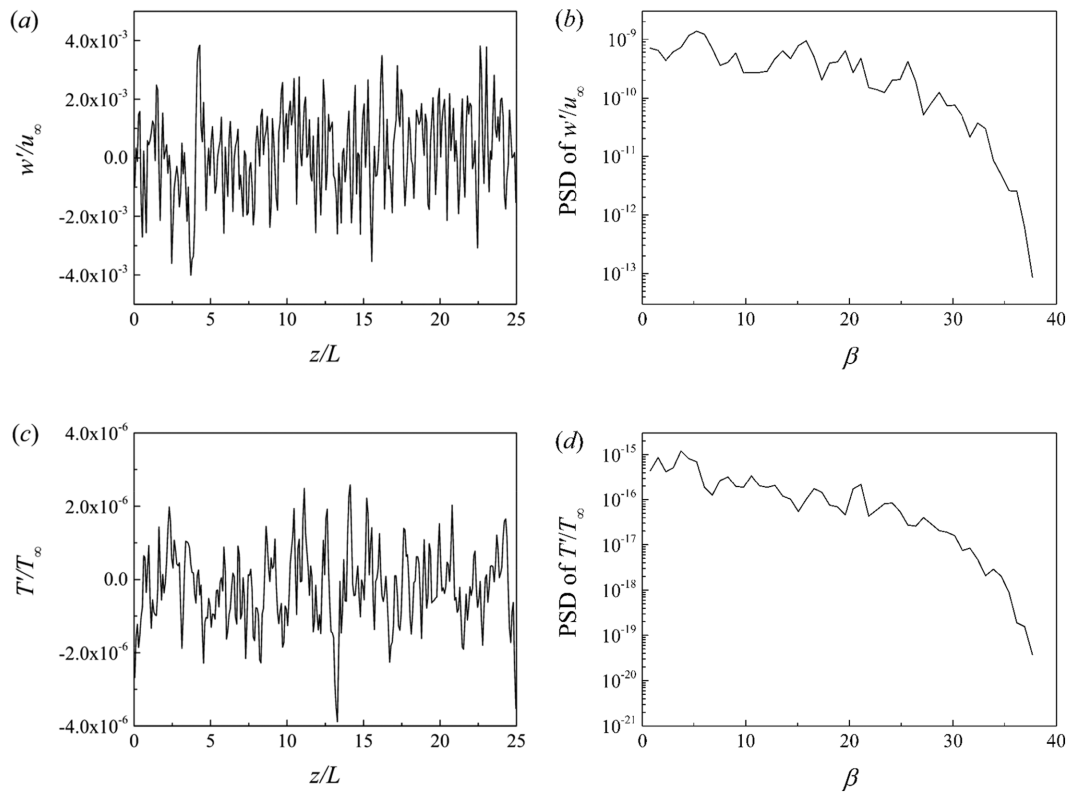


FIG. 15. (a) Normalized spanwise velocity perturbation across the z -direction at $\xi/L = 48.7$ ($j = 1$). (b) Power spectral density (PSD) of (a) vs β . (c) Normalized temperature perturbation across the z -direction at $\xi/L = 48.7$ ($j = 1$). (d) PSD of (c) vs β .

random number ranging from 0 to 1. Because β_{\max} is near 2.5 in the baseline case according to the resolvent analysis [i.e., Fig. 7(a)], 300 grids are constructed in the spanwise direction of the 3D computational domain with a width of 25 mm. Analogous to the setting in the resolvent analysis, A_f is set as 0.01 at $\xi/L = 48.7$ with $1 \leq j \leq 300$ and $1 \leq k \leq 300$, such that the linear instability could be excited within the region of interest. A periodic boundary condition is set at the z interfaces. The perturbations in Eq. (17) are enforced continuously until a quasisteady state is reached downstream. It should be noted that the optimal forcing in the form of normal modes used in the resolvent analysis does not typically exist in practical applications. Nevertheless, the range of the most amplified spanwise numbers obtained from the resolvent analysis still provides valuable information for stability analysis and will be further demonstrated through the numerical simulations discussed in this section. For the fast Fourier transform (FFT) analysis, Welch's method⁶⁰ with three segments and 50% overlap is applied to analyze the data obtained in the 3D simulation. A Hamming window is used on each segment for weighting the data.

Figure 15 shows the normalized spanwise velocity and temperature perturbation introduced by the random forcing at $\xi/L = 48.7$ with $j = 1$ (just above the wall). The PSD results indicated that broadband upstream disturbances are excited from $\beta = 0$ to 37. We anticipated that the most unstable Görtler instability would be selected “naturally” at the downstream location. Figure 16 shows the distribution of the skin friction coefficient across the streamwise direction

with or without random forcing. The skin friction coefficient is defined as follows:

$$C_f = \frac{\tau_w}{0.5 \rho_\infty u_\infty^2}, \quad (18)$$

where τ_w is the surface shear stress. Due to the presence of upstream disturbance, the surface shear stress oscillates along the spanwise direction and is amplified across the streamwise direction. Eventually, the instability is fully developed downstream with a higher average C_f

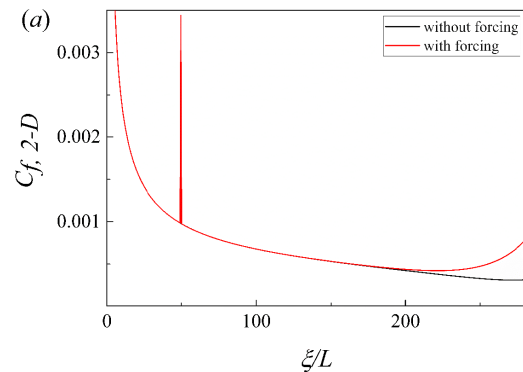


FIG. 16. Distribution of spanwise (or 2D) averaged skin friction coefficient across the ξ -direction with and without random forcing.

compared with the case without forcing (i.e., when $\xi/L > 200$), as shown in Fig. 16. The abrupt increase in $C_{f,2D}$ in Fig. 16 at approximately $\xi/L = 48.7$ is attributed to the random forcing, as a spanwise velocity perturbation [i.e., Eq. (17)] is always implemented at this specified ξ/L . The spanwise component contributes to the surface shear stress, and the additional perturbation at the designated ξ/L location results in the sudden increase in $C_{f,2-D}$.

To justify the evolution of the Görtler instability across the streamwise direction, the root mean square (rms) of the spanwise velocity is calculated as follows:

$$\sigma_w = \sqrt{\frac{1}{N_\eta N_z} \sum_{j=1}^{N_\eta} \sum_{k=1}^{N_z} \left(\frac{w}{u_\infty} \right)^2}, \quad (19)$$

where N_η and N_z are the numbers of grid cells in the η and z directions, respectively. The spatial history of $\ln(\sigma_w/\sigma_0)$ is shown in Fig. 17. The increasing r.m.s. of the spanwise velocity recorded downstream implies that the instability is amplified across the streamwise direction. The growth rate of σ_w agrees with the slope of the N factor [i.e., calculated by Eq. (13)] from the resolvent analysis at $\beta = 2.3$ (the most unstable β for this baseline case), indicating that the regions of interest in the simulation are at the linear stage.

Figure 18 shows the contours of the streamwise velocity and the spanwise velocity downstream of the concave wall from the 3D simulation and the resolvent analysis, respectively. To acquire the contours from the resolvent analysis, Eq. (6) is used and the perturbation quantity is described below:

$$U'(x, y, z, t) = A_{RA} \hat{U}_{2-D}(x, y) \exp(i\beta z), \quad (20)$$

where $\hat{U}_{2-D}(x, y)$ is the 2D eigenfunction from the optimal response and A_{RA} is the perturbation amplitude and can be set arbitrary (i.e., in this case, $A_{RA} = 2.0 \times 10^{-4}$ is used). The similar vortical structure in Figs. 18(a) and 18(b) [or Figs. 18(c) and 18(d)] at $z/L = 20$ –23 implies that the 3D simulation could capture the mode near $\beta = 2.3$ under stochastic forcing. However, due to the presence of broadband wavenumbers in the simulation, downstream contours exhibit

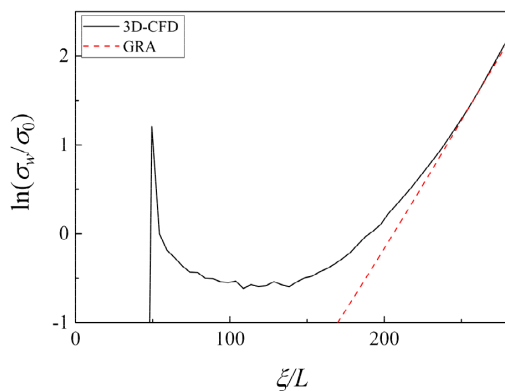


FIG. 17. Spatial history of the root mean square of the spanwise velocity. The dashed-dotted line denotes the slope of the N factor at $\beta = 2.3$ from the resolvent analysis.

irregular streamwise vortices with varying spanwise scales rather than regular structures with $\beta = 2.3$ (also shown later in the FFT analysis in Fig. 20). Nevertheless, the averaged spanwise wavelength in the simulation is comparable to that in the resolvent analysis. The comparison between Figs. 18(a) and 18(c) reveals that the counterrotating vortical structures increase in size downstream, and some become visible as complete vortices (i.e., near $z/L = 10$ at $\xi/L = 247.1$). The flow structure remains relatively unchanged between the two slices at the selected ξ/L locations overall, again suggesting that the instability is linearly amplified across the streamwise direction.

In addition, streamwise heat-flux streaks are captured in the CFD when random forcing is implemented. A wall Stanton number is defined as follows:

$$St = \frac{q_w}{0.5\rho_\infty u_\infty^3}, \quad (21)$$

where q_w is the surface heat flux. Figure 19 shows the instantaneous distributions of the skin friction coefficient and wall Stanton number. Streamwise shear-stress streaks and heat-flux streaks at the quasisteady state are observed on the concave wall downstream. Therefore, the regions of interest for the spectral estimation are set between $\xi/L = 90$ and 250 based on the CFD results.

The FFT analysis of the skin friction coefficient and wall Stanton number obtained from the 3D simulation is presented in Fig. 20. Apparently, the signal from the high spanwise number component (i.e., $\beta > 3$) drops dramatically, indicating that the Görtler instability is not excited in that range. The most unstable β exists in a range from 0.75 to 2.3, while that from the resolvent analysis shows a marginally larger β_{\max} at 2.3. This slight difference can be attributed to the different forcing strategies in the resolvent analysis and the 3D simulation. The stochastic forcing in the latter case allows the development of the “natural” instability under the free-stream disturbance environment,⁵⁹ which is closer to the actual receptivity process observed in the experiments. Unlike in the resolvent analysis, where discrete β ranges are tested for the optimal response [i.e., Eq. (8)], the broadband spanwise wavelength is not discrete under the random forcing [spatial white noise in Eq. (17)]. Therefore, the most unstable β is presented in ranges instead of a specific value in the simulations. Overall, the resolvent analysis can capture the Görtler instability that exists in the 3D simulation under random forcing. The conclusions on the geometric and flow parameters change by the resolvent analysis are verified.

V. CONCLUSIONS

In this study, the stationary Görtler instability at the linear state in the boundary layer over a concave wall was investigated through the variation of geometric and flow parameters. The resolvent analysis and the LST were used, and a 3D numerical simulation on the baseline case was conducted for verification. A new dimensionless wavelength parameter was proposed.

The geometric parameters pertaining to the concave wall include the radius of curvature and the turning angle. Based on the resolvent analysis and the LST, the increase in radius of curvature stabilized the Görtler instability as reported in the literature. On the other hand, the turning angle had a negligible effect on the enhancement of Görtler instability, as it only affected the length of the concave surface. In terms of flow conditions, the Görtler instability was stabilized at low Reynolds number, due to the thickening of the boundary layer at low density.

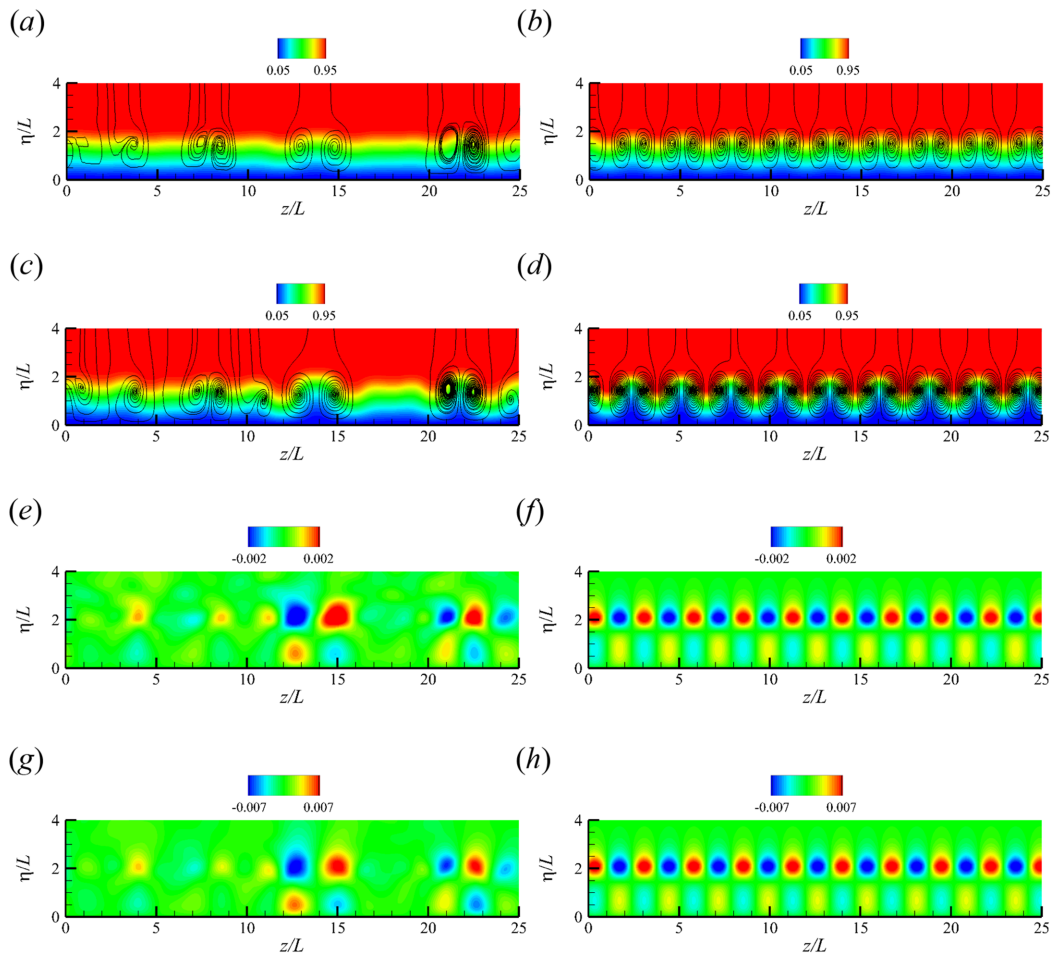


FIG. 18. Contours of the streamwise velocity [(a)–(d)] and the spanwise velocity [(e)–(h)] at $\xi/L = 197.7$ [(a), (b), (e), and (f)] and 247.1 [(c), (d), (g), and (h)]. (a), (c), (e), and (g) are obtained from the 3D simulation, while (b), (d), (f), and (h) are obtained from the resolvent analysis at $\beta = 2.3$ [refer to Eq. (20)]. The solid line superimposed in a to d denotes the in-plane streamlines.

The wall cooling effect destabilized the Görtler instability by reducing the boundary layer thickness, in agreement with previous findings. The change in Mach number had marginal effect on the Görtler instability, which can be attributed to the severe adverse pressure gradient (manifested in terms of an inflection point within the boundary layer) in the low Mach number case; thus, the boundary layer thickness in the selected case shows little change. In addition, the absence of a receptivity process may have contributed to this insensitivity. A new dimensionless wavelength parameter was proposed to consider the wall temperature effect in compressible flows, providing a preliminary prediction of the most unstable spanwise wavenumber based on the given geometric and flow properties.

Finally, a 3D numerical simulation was conducted by enforcing a random perturbation on the spanwise velocity. The most unstable spanwise wavenumber obtained is near the case computed by the resolvent analysis, which further verifies the stability analysis discussed in this paper.

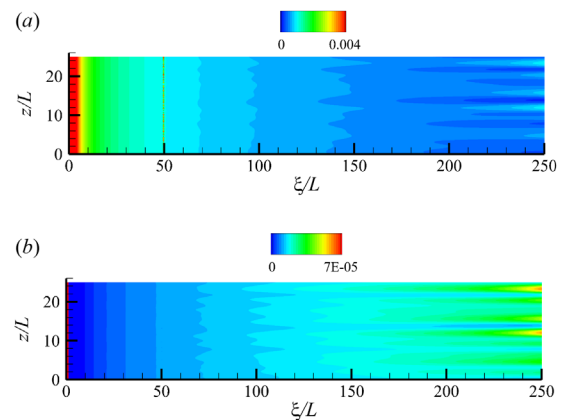


FIG. 19. Instantaneous distributions of the (a) skin friction coefficient and (b) wall Stanton number. Random forcing is implemented at $\xi/L = 48.7$.

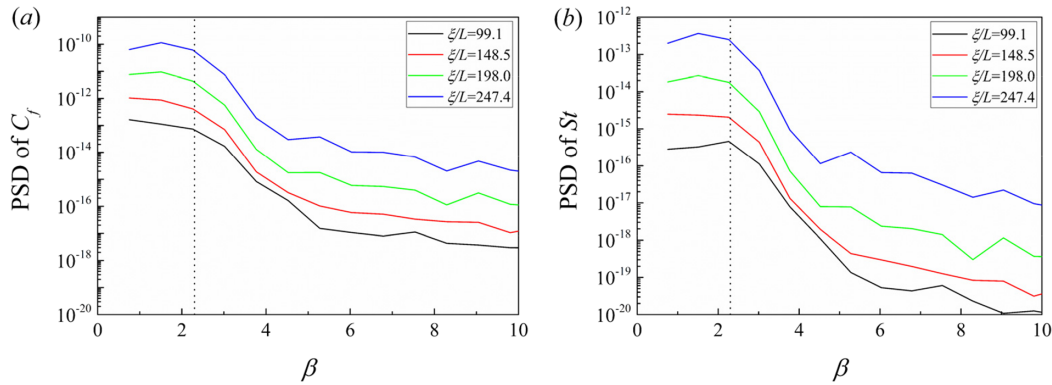


FIG. 20. PSD of (a) skin friction coefficient and (b) wall Stanton number at different ξ/L . The vertical dotted line indicates the β_{\max} from the resolvent analysis.

This study describes the change in geometric and flow conditions on the Görtler instability in the linear state over a concave wall and contributes to the prediction of this type of instability in related scenarios.

ACKNOWLEDGMENTS

This study was supported by the Hong Kong Research Grants Council (Nos. 15216621 and 15217622).

AUTHOR DECLARATIONS

Conflict of Interest

The authors have no conflicts to disclose.

Author Contributions

Ken Chun Kit Uy: Conceptualization (equal); Data curation (equal); Formal analysis (equal); Investigation (equal); Methodology (equal); Validation (equal); Writing – original draft (equal); Writing – review & editing (equal). **Jiaao Hao:** Conceptualization (equal); Data curation (equal); Investigation (equal); Methodology (equal); Project administration (equal); Resources (equal); Software (equal); Supervision (equal); Writing – review & editing (equal). **Chih-Yung Wen:** Conceptualization (equal); Funding acquisition (equal); Project administration (equal);

Resources (equal); Supervision (equal); Writing – review & editing (equal).

DATA AVAILABILITY

The data that support the findings of this study are available from the corresponding author upon reasonable request.

APPENDIX: GRID CONVERGENCE STUDY

The computational domain of the baseline case is constructed with a total of 600 and 300 nodes in the ξ and η directions, respectively. The arc length $D = 296.6$ mm and the maximum η is 50 mm at each ξ position (Fig. 1). Two levels of resolution are considered, including a standard mesh of 600×300 and a finer mesh of 900×400 . Approximately 200 (250) grid points are located within the boundary layer for the standard (finer) mesh. Both numerical simulation and resolvent analysis are performed on these grids to verify the grid convergence.

Figure 21 shows the distributions of the skin friction coefficient C_f and the wall pressure coefficient C_p obtained at different grid resolutions for the baseline case. The wall pressure coefficient C_p is defined as follows:

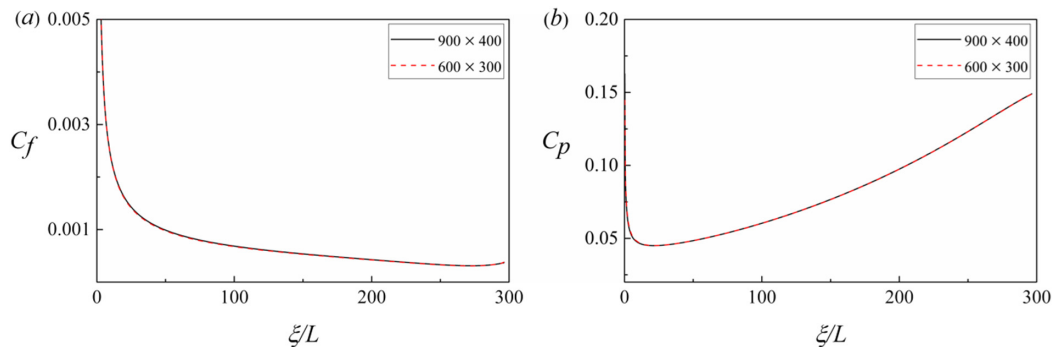


FIG. 21. Distributions of the (a) skin friction coefficient and (b) wall pressure coefficient obtained at different grid resolutions for the baseline case.

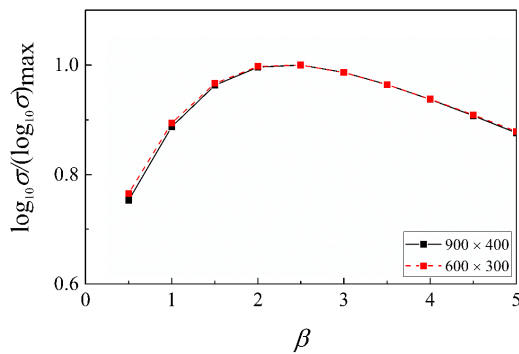


FIG. 22. Optimal gain (normalized to maintain the unit maximum value) from the resolvent analysis of the baseline case on different grid resolutions. Forcing is implemented at $\xi/L = 48.7$ for the entire η plane with $\omega = 0$.

$$C_p = \frac{p_w}{0.5\rho_\infty u_\infty^2}, \quad (\text{A1})$$

where p_w is the wall pressure. The overlapping of the two profiles with different resolutions indicated that the standard grid is adequate for the numerical simulation.

Figure 22 compares the optimal gain obtained from the resolvent analysis using the 2D base flow profiles computed by the two meshes. The most unstable mode range is captured in both meshes, showing that the standard grid is sufficiently accurate for the stability analysis.

REFERENCES

- ¹P. Hall, "Görtler vortices in growing boundary layers: The leading edge receptivity problem, linear growth and the nonlinear breakdown stage," *Mathematika* **37**, 151 (1990).
- ²J. M. Floryan, "On the görtler instability of boundary layers," *Prog. Aerosp. Sci.* **28**, 235 (1991).
- ³W. S. Saric, "Görtler vortices," *Annu. Rev. Fluid Mech.* **26**, 379 (1994).
- ⁴F. Li, M. Choudhari, C.-L. Chang, P. Greene, and M. Wu, *Development and Breakdown of Gortler Vortices in High Speed Boundary Layers* (American Institute of Aeronautics and Astronautics, 2010).
- ⁵L. De Luca, G. Cardone, D. Aymer de la Chevalerie, and A. Fonteneau, "Goertler instability of a hypersonic boundary layer," *Exp. Fluids* **16**, 10 (1993).
- ⁶L. Ciolkosz and E. Spina, *An Experimental Study of Görtler Vortices in Compressible Flow* (American Institute of Aeronautics and Astronautics, 2006).
- ⁷G. Huang, W. Si, and C. Lee, "Early stage evolution of naturally developing Görtler streaks," *Phys. Fluids* **33**, 061706 (2021).
- ⁸G. Huang, W. Si, and C. Lee, "Inner structures of Görtler streaks," *Phys. Fluids* **33**, 034116 (2021).
- ⁹G. Huang, "Interactions between Görtler vortices and the second mode in hypersonic boundary layer," *Phys. Fluids* **33**, 111701 (2021).
- ¹⁰X. Li, Y. Zhang, H. Yu, Z.-K. Lin, H.-J. Tan, and S. Sun, "Görtler vortices behavior and prediction in dual-incidence shock-wave/turbulent-boundary-layer interactions," *Phys. Fluids* **34**, 106103 (2022).
- ¹¹C. Whang and X. Zhong, *Secondary Goertler Instability in Hypersonic Boundary Layers* (American Institute of Aeronautics and Astronautics, 2001).
- ¹²J. Ren and S. Fu, "Secondary instabilities of Görtler vortices in high-speed boundary layer flows," *J. Fluid Mech.* **781**, 388 (2015).
- ¹³X. Chen, G. L. Huang, and C. B. Lee, "Hypersonic boundary layer transition on a concave wall: Stationary Görtler vortices," *J. Fluid Mech.* **865**, 1–40 (2019).
- ¹⁴X. Chen, J. Chen, X. Yuan, G. Tu, and Y. Zhang, "From primary instabilities to secondary instabilities in Görtler vortex flows," *Adv. Aerodyn.* **1**, 19 (2019).
- ¹⁵R. Song, L. Zhao, and Z. Huang, "Secondary instability of stationary Görtler vortices originating from first/second Mack mode," *Phys. Fluids* **32**, 034109 (2020).
- ¹⁶G. Huang, X. Chen, J. Chen, X. Yuan, and G. Tu, "The stabilizing effect of grooves on Görtler instability-induced boundary layer transition in hypersonic flow," *Phys. Fluids* **35**, 041701 (2023).
- ¹⁷X. Chen, J. Chen, and X. Yuan, "Hypersonic boundary layer transition on a concave wall induced by low-frequency blowing and suction," *Phys. Fluids* **34**, 114105 (2022).
- ¹⁸F. Li, M. Choudhari, and P. Paredes, "Secondary instability of Görtler vortices in hypersonic boundary layer over an axisymmetric configuration," *Theor. Comput. Fluid Dyn.* **36**, 205 (2022).
- ¹⁹P. Hall, "Taylor—Görtler vortices in fully developed or boundary-layer flows: Linear theory," *J. Fluid Mech.* **124**, 475 (1982).
- ²⁰P. Hall, "The linear development of Görtler vortices in growing boundary layers," *J. Fluid Mech.* **130**, 41 (1983).
- ²¹A. P. Bassom and P. Hall, "The receptivity problem for O(1) wavelength Görtler vortices," *Proc. R. Soc. A* **446**, 499 (1994).
- ²²X. Wu, D. Zhao, and J. Luo, "Excitation of steady and unsteady Görtler vortices by free-stream vortical disturbances," *J. Fluid Mech.* **682**, 66 (2011).
- ²³S. Viaro and P. Ricco, "Compressible unsteady Görtler vortices subject to free-stream vortical disturbances," *J. Fluid Mech.* **867**, 250 (2019).
- ²⁴S. Viaro and P. Ricco, "Neutral stability curves of compressible Görtler flow generated by low-frequency free-stream vortical disturbances," *J. Fluid Mech.* **876**, 1146 (2019).
- ²⁵A. Bottaro and P. Luchini, "Görtler vortices: Are they amenable to local eigenvalue analysis?," *Eur. J. Mech.-B/Fluids* **18**, 47 (1999).
- ²⁶J. Ren and S. Fu, "Study of the discrete spectrum in a Mach 4.5 Görtler flow," *Flow, Turbul. Combust.* **94**, 339 (2015).
- ²⁷J. M. Floryan, "The second mode of the Goertler instability of boundary layers," *AIAA J.* **23**, 1828 (1985).
- ²⁸R. E. Spall and M. R. Malik, "Goertler vortices in supersonic and hypersonic boundary layers," *Phys. Fluids A* **1**, 1822 (1989).
- ²⁹P. J. Schmid, "Nonmodal stability theory," *Annu. Rev. Fluid Mech.* **39**, 129 (2007).
- ³⁰P. Paredes, M. M. Choudhari, and F. Li, "Instability wave-streak interactions in a supersonic boundary layer," *J. Fluid Mech.* **831**, 524 (2017).
- ³¹C. Cossu, J. M. Chomaz, P. Huerre, and M. Costa, "Maximum spatial growth of Görtler vortices," *Flow, Turbul. Combust.* **65**, 369 (2000).
- ³²F. Li, M. M. Choudhari, P. Paredes, S. P. Schneider, and P. Portoni, *Görtler Instability and Its Control via Surface Suction over an Axisymmetric Cone at Mach 6* (American Institute of Aeronautics and Astronautics, 2018).
- ³³A. Dwivedi, G. S. Sidharth, J. W. Nichols, G. V. Candler, and M. R. Jovanović, "Reattachment streaks in hypersonic compression ramp flow: An input-output analysis," *J. Fluid Mech.* **880**, 113 (2019).
- ³⁴A. Dwivedi, S. Gs, C. Hollender, and G. V. Candler, *Input-Output Analysis for Görtler-Type Instability in Axisymmetric Hypersonic Boundary-Layers* (American Institute of Aeronautics and Astronautics, 2020).
- ³⁵A. Dwivedi, G. S. Sidharth, and M. R. Jovanović, "Oblique transition in hypersonic double-wedge flow," *J. Fluid Mech.* **948**, A37 (2022).
- ³⁶B. Bugeat, J. C. Chassaing, J. C. Robinet, and P. Sagaut, "3D global optimal forcing and response of the supersonic boundary layer," *J. Comput. Phys.* **398**, 108888 (2019).
- ³⁷B. Bugeat, J. C. Robinet, J. C. Chassaing, and P. Sagaut, "Low-frequency resolvent analysis of the laminar oblique shock wave/boundary layer interaction," *J. Fluid Mech.* **942**, A43 (2022).
- ³⁸D. Sipp, O. Marquet, P. Meliga, and A. Barbagallo, "Dynamics and control of global instabilities in open-flows: A linearized approach," *Appl. Mech. Rev.* **63**, 030801 (2010).
- ³⁹H. Bippes, Experimental study of the laminar-turbulent transition of a concave wall in a parallel flow," NTRS-NASA Tech. Report No. NASA-TM-75243 (1978), see <https://ntrs.nasa.gov/citations/19780013469>.
- ⁴⁰J. M. Floryan and W. S. Saric, "Stability of Gortler Vortices in Boundary Layers," *AIAA J.* **20**, 316 (1982).
- ⁴¹J. Hao and C.-Y. Wen, "Stabilization of a two-dimensional hypersonic boundary layer using a shallow cavity," *AIAA J.* (published online).

- ⁴²J. Hao, J. Fan, S. Cao, and C.-Y. Wen, “Three-dimensionality of hypersonic laminar flow over a double cone,” *J. Fluid Mech.* **935**, A8 (2022).
- ⁴³R. W. McCormack, *Numerical Computation of Compressible and Viscous Flow* (American Institute of Aeronautics and Astronautics, Inc., 2014).
- ⁴⁴B. van Leer, “Towards the ultimate conservative difference scheme. V. A second-order sequel to Godunov’s method,” *J. Comput. Phys.* **32**, 101 (1979).
- ⁴⁵M. J. Wright, G. V. Candler, and D. Bose, “Data-parallel line relaxation method for the Navier-Stokes equations,” *AIAA J.* **36**, 1603 (1998).
- ⁴⁶J. Ren and S. Fu, “Competition of the multiple Görtler modes in hypersonic boundary layer flows,” *Sci. China* **57**, 1178 (2014).
- ⁴⁷G. Guennebaud, B. Jacob *et al.*, “Eigen v3” (2010), see https://eigen.tuxfamily.org/index.php?title=Main_Page.
- ⁴⁸J. Hao, S. Cao, C.-Y. Wen, and H. Olivier, “Occurrence of global instability in hypersonic compression corner flow,” *J. Fluid Mech.* **919**, A4 (2021).
- ⁴⁹B.-T. Chu, “On the energy transfer to small disturbances in fluid flow (Part I),” *Acta Mech.* **1**, 215 (1965).
- ⁵⁰A. Hanifi, P. J. Schmid, and D. S. Henningson, “Transient growth in compressible boundary layer flow,” *Phys. Fluids* **8**, 826 (1996).
- ⁵¹D. Sipp and O. Marquet, “Characterization of noise amplifiers with global singular modes: The case of the leading-edge flat-plate boundary layer,” *Theor. Comput. Fluid Dyn.* **27**, 617 (2013).
- ⁵²D. Sorensen, R. Lehoucq, C. Yang, and K. J. Maschhoff, *ARPACK Software* (1996–2008), see <https://epubs.siam.org/doi/book/10.1137/1.9780898719628>.
- ⁵³X. S. Li, J. W. Demmel, J. R. Gilbert, and L. Grigori, “SuperLU users’ guide,” Tech report LBNL-44289 (1999), see https://scholar.google.com/citations?view_op=view_citation&hl=zh-TW&user=Bjpb27sAAAAJ&citation_for_view=Bjpb27sAAAAJ:ULOm3_A8WrAC.
- ⁵⁴J. van Ingen, *The eN Method for Transition Prediction. Historical Review of Work at TU Delft* (American Institute of Aeronautics and Astronautics, 2008).
- ⁵⁵M. T. Landahl, “A note on an algebraic instability of inviscid parallel shear flows,” *J. Fluid Mech.* **98**, 243 (1980).
- ⁵⁶S. Winoto, T. Tandiono, D. Shah, and H. Mitsudharmadi, “Concave surface boundary layer flows in the presence of streamwise vortices,” *Int. J. Fluid Mach. Syst.* **4**, 33 (2011).
- ⁵⁷Q.-C. Wang, Z.-G. Wang, and Y.-X. Zhao, “Visualization of Görtler vortices in supersonic concave boundary layer,” *J. Visualization* **21**, 57 (2018).
- ⁵⁸S. Unnikrishnan and D. V. Gaitonde, “Interactions between vortical, acoustic and thermal components during hypersonic transition,” *J. Fluid Mech.* **868**, 611 (2019).
- ⁵⁹C. Hader and H. F. Fasel, “Towards simulating natural transition in hypersonic boundary layers via random inflow disturbances,” *J. Fluid Mech.* **847**, R3 (2018).
- ⁶⁰P. Welch, “The use of fast Fourier transform for the estimation of power spectra: A method based on time averaging over short, modified periodograms,” *IEEE Trans. Audio Electroacoust.* **15**, 70 (1967).